Modeling wave propagation in Sandwich Composite Plates for Structural Health Monitoring

V. N. Smelyanskiy[1], V. Hafiychuk[1], D. G. Luchinsky[1], R. Tyson[2], J. Miller[3], C. Banks[3]

[1] *NASA Ames Research Center, Mail Stop 269-2, Moffett Field, CA 94035, USA*

vadim.n.smelyanskiy@nasa.gov

[2] *University of Alabama,1804, Sparkman Dr., Huntsville, AL, 35816, USA*

Richard.Tyson@nasa.gov

[3] *Marshal Space Flight Center/EM20, Huntsville, AL, 35812, USA*

jim.miller@nasa.gov

ABSTRACT

Wave propagation is investigated in sandwich composite panels using analytical approach for layered materials, Mindlin plate theory and finite element modeling in the context of developing an on-board structural health monitoring system. It is shown that theoretical results are in agreement with the results of numerical simulations and with experimental results.

1. INTRODUCTION

Composite sandwich panels (CSP), consisting of fiber-reinforced facesheets separated by low-density cores, offer lightweight and flexible production capabilities and high performance: high strength, damage tolerance and thermal resistance (Zenkert, 1995),(Zenkert, 1997). During the past few decades, the CSPs have been steadily replacing the traditional materials in many industries including e.g. automotive, marine, and aerospace. Their stiffness-to-weight ratios and damage tolerance are especially attractive in aerospace industry leading to higher payloads (Bednarcyk, Arnold, Collier, & Yarrington, 2007). However, the multi-layered construction and laminate layup of the facesheets allow for debonding, delamination, and other internal flaws that are hardly visible and may severely damage the structural strength of the CSPs. In this context, it becomes important to develop reliable on-line structural health monitoring (SHM) systems of the composite panels. The aerospace industry has one of the highest payoffs for SHM since damage can lead to catastrophic failures.

There are several techniques currently under investigation (See, for example,(Raghavan & Cesnik, 2007)) for diagnostics including e.g. embedded fiber optic sensors for strain measurement, active ultrasonics, passive acoustic emission monitoring, and electromechanical impedance measurements. The Lamb wave based diagnostics of CSPs is one of the most promising SHM techniques due to the similarity between the Lamb wavelength and the CSP thickness, the ability to travel far distances, high sensitivity, active sensing and low cost of piezoelectric wafer actuators/sensors (Raghavan & Cesnik, 2007). The development of the reliable SHM technique based on guided wave propagation in CSPs is complicated due to heterogeneity of the sandwich structures. This study is needed for better understanding and more reliable model predictions in the context of development of the in-flight SHM for the next generation of the heavy-lift vehicle.

2. MODELING WAVE PROPAGATION

A three-dimensional formulation relying on a global matrix technique provides a general framework for analysis of wave propagation in an anisotropic multi-layered medium (Zakharov, 2008). We consider symmetrical sandwich structures and the equation of motion in each layer reads

$$\partial_p \sigma^j_{mp} + \rho_j \omega^2 u_m = 0, \quad m,p,j = 1,2,3. \tag{1}$$

where for j-th layer ρ_j is the density. For an isotropic material the stresses σ^j_{mp} and strains ε^j_{mp} satisfy Hook's law and Kelvin–Voigt model of linear viscoelasticity and constitutive relations have the form

$$\sigma^j_{mp} = (\lambda'_j + \lambda''_j \partial_t)\delta_{mp}\varepsilon^j_{kk} + 2(\mu'_j + \mu''_j \partial_t)\varepsilon^j_{mp}.$$

For small displacements $u^{(n)}_j$ components of the deformation matrix $\varepsilon^{(n)}_{mp}$ are given by the following relation

$$\varepsilon^j_{mp} = \frac{1}{2}\left(\partial_p u^j_m + \partial_m u^j_p\right),$$

For the complex-valued representation of Lame constants, wave speeds

$$\lambda_j = \lambda'_j - i\omega\lambda''_j, \mu_j = \mu'_j - i\omega\mu''_j. \tag{2}$$

$$c_p^j = \sqrt{\frac{(\lambda_j + 2\mu_j)}{\rho_j}} = \sqrt{\frac{E_j(1-\nu_j)}{\rho_j(1+2\nu_j)(1-2\nu_j)}} = \alpha|_j, \quad (3)$$

$$c_s^j = \sqrt{\mu_j/\rho_j} = \sqrt{E_j/2\rho_j(1+\nu_j)} = \beta|_j, \quad (4)$$

$$k_p^j = \omega/c_p^j, k_s^j = \omega/c_s^j. \quad (5)$$

where material parameters $\alpha, \beta, \mu, \lambda E, \rho, \nu$ correspond to each layer $j = 1, 2, 3$.

The three-dimensional formulation assumes the continuity of displacements u_j and components of stress tensor σ_{ij} on the inner boundaries of the layers and allows for a quite general form of the boundary conditions. For the circular plate PZT sensors exiting dynamic stresses at a circular source could be considered symmetrical about its axis (0Z) and on the interfaces $x_3 = z_j, j = 1, 2, 3$.

Let's consider an infinite sandwich panel for theoretical modeling and square panel for FE simulation. The cylindrical coordinates (r, θ, z) are used for consideration where zeros of z-axis coincide with the midplane of the panel. In the simplest case due to axisymmetry the solution problem is two dimensional in coordinates (r, z) (Zakharov, 2008)

$$u_r^j = \left[-u^j B_n'(sr) + w^j \frac{n}{kr} B_n(sr)\right] \left\{ \begin{array}{c} \cos n\theta \\ -\sin n\theta \end{array} \right\}, \quad (6)$$

$$u_\theta^j = \left[u^j \frac{n}{kr} B_n(sr) - w^j B_n'(sr)\right] \left\{ \begin{array}{c} \cos n\theta \\ -\sin n\theta \end{array} \right\}, \quad (7)$$

$$u_z^j = v^j B_n(sr) \left\{ \begin{array}{c} \cos n\theta \\ -\sin n\theta \end{array} \right\}. \quad (8)$$

where the first or second term could be chosen in the French brackets, so they represent the terms in the trigonometrical Fourier series wrt θ. The terms B_n=$B_n(sr)$ are any of the appropriate Bessel function or Hankel function of the first or second kind and $B' = dB_n(sr)/d(sr)$,

$$\left[\begin{array}{c} u^j \\ v^j \end{array} \right] = A_L^{+j} \left[\begin{array}{c} \cos C_\alpha z \\ \frac{C_\alpha^j}{k} \sin C_\alpha z \end{array} \right] + A_L^{-j} \left[\begin{array}{c} \sin C_\alpha z \\ -\frac{C_\alpha^j}{k} \cos C_\alpha z \end{array} \right]$$

$$+A_S^{+j} \left[\begin{array}{c} -\frac{C_\beta^j}{k} \cos C_\beta z \\ \sin C_\beta z \end{array} \right] + A_S^{-j} \left[\begin{array}{c} \frac{C_\beta^j}{k} \sin C_\beta z \\ \cos C_\beta z \end{array} \right], \quad (9)$$

$$w^j = B_S^{+j} \cos C_\alpha z + B_S^{-j} \sin C_\beta z. \quad (10)$$

where $A_{L,S}^{\pm j}$, $B_S^{\pm j}$ are constants and displacement components are composed of symmetrical and anti-symmetrical terms according to $z = 0$, which are corresponding to symmetrical and anti-symmetrical modes, respectively. For the homogeneous material properties the general approach outlined above can be simplified allowing for further analytical treatment of the problem of finding dispersion relations of the sandwich panel (Zakharov, 2008),(Lowe, 1995). Accordingly, the Lamb wave dispersion relations are determined by the determinant of square matrix of the 16x16 order

$$\det \left[\begin{array}{cccc} [D_{0b}] & [-D_{1t}] & & \\ & [D_{1b}] & [-D_{2t}] & \\ & & [D_{2b}] & [-D_{3t}] \\ & & & [D_{3b}] \quad [-D_{0t}] \end{array} \right] = 0, \quad (11)$$

where the D matrices for the top (index t) and bottom (index b) of a layer can be expressed, respectively, as

$$D_{jt} = \left[\begin{array}{cccc} s & sg_\alpha & C_\beta & -C_\beta g_\beta \\ C_\alpha & -C_\alpha g_\alpha & -s & -sg_\beta \\ i\rho B & i\rho B g_\alpha & -p_\beta C_\beta & p_\beta C_\beta g_\beta \\ p_\alpha C_\alpha & -p_\alpha C_\alpha g_\alpha & i\rho B & i\rho B g_\beta \end{array} \right]_j, \quad (12)$$

$$D_{jb} = \left[\begin{array}{cccc} sg_\alpha & s & C_\beta g_\beta & -C_\beta \\ C_\alpha g_\alpha & -C_\alpha & -sg_\beta & -s \\ i\rho B g_\alpha & i\rho B & -p_\beta C_\beta g_\beta & p_\beta C_\beta \\ p_\alpha C_\alpha g_\alpha & -p_\alpha C_\alpha & i\rho B g_\beta & i\rho B \end{array} \right]_j, \quad (13)$$

where $j = 0$ corresponds to air, s is the wave number in the direction of wave propagation,

$$p_\alpha = 2i\rho s\alpha^2, p_\beta = 2i\rho s\beta^2,$$

$$C_\alpha = (\omega^2/\alpha^2 - s^2)^{1/2}, C_\beta = (\omega^2/\beta^2 - s^2)^{1/2},$$

$$g_\alpha = e^{iC_\alpha z}, g_\beta = e^{iC_\beta z}, B = \omega^2 - 2\beta^2 s^2.$$

All matrices in (11) are 4×4 except D_{0b} and D_{0t} which are 4×2.

Let us investigate dispersion curves for typical sandwich structure with soft core about 1in in thickness and carbon fibre reinforced plastic facesheet consisting of 14 ply. The velocities are determined by the geometry of the structure as well as longitudinal and shear velocities characterizing materials. In the simulations we used CFRP face sheets with Young modulus 60GPa, Poisson ratio 0.3 and density 1500kg/m^{3}and homogenized core with Young modulus E=80MPa, the same Poisson ratio and density was 100kg/m^3. As a result, longitudinal velocity was 7338m/s and 1038m/s and shear velocity 3922 and 555m/s, correspondingly. These velocities are plotted by green dashed lines. The spectrum of the waves (9),(10) is presented in Figure 1 and 2 for the case when the core of the sandwich $(j = c)$ is much softer than for the facesheet. The vibration of the soft core is restricted by rigid surfaces of the face sheet and we have many local modes in the structure. The dispersion curves change very drastically if the sandwich core is visc oelastic. Many curves corresponding to honeycomb core just disappear (Figure 2) and for the case when the real and imaginary parts of the elastic module become comparable the propagation is determined by facesheet modes.

Analyzing dispersion plots for low velocities we can see that at at low velocities dispersion curves are modulated by facesheet flexural velocity. At higher frequency these curves tend to shift to shear velocity of the core. For high velocities dispersion curves exhibit a set of vertical paths where phase

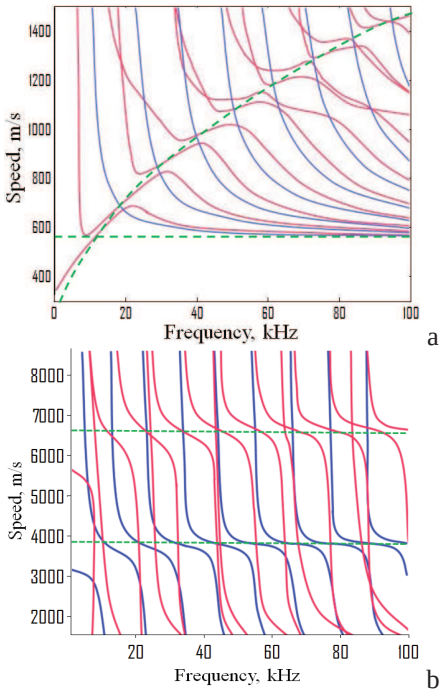

Figure 1: Dispersion curves of Lamb wave of phase velocities with respect to frequency for symmetric sandwich, (a) – low speed limit and (b) – high speed limit, blue lines - shear waves, lilac lines - Lamb waves).

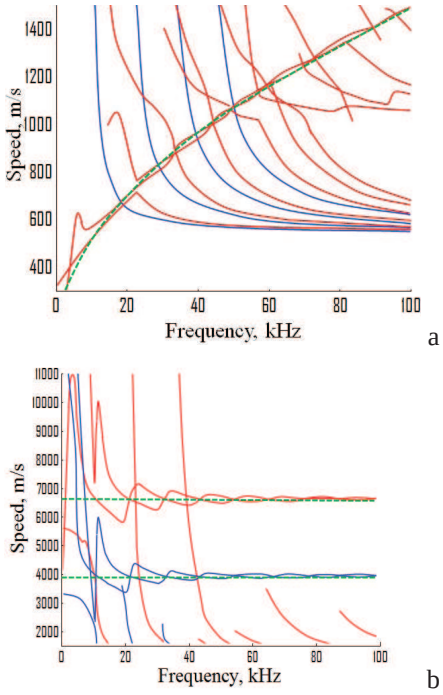

Figure 2: Dispersion curves of Lamb wave of phase velocities with respect to frequency for symmetric sandwich with viscoelastic core $\lambda_c' = 0.1\lambda_c$, $\mu_c' = 0.1\mu_c$; (a) – low speed limit, and (b) – high speed limit. Blue lines - shear waves, lilac lines - Lamb waves.

velocity changes by a large value at the same frequency. The group velocity at these frequencies (vertical lines) is close to zero and this means waves are practically standing. This statements is confirmed by FE simulations.

If the core is viscoelastic we have coupling of different modes and the dispersion curves start to intersect, some of the modes vanish and some of them change their trend with increasing frequency (Fig. 2). With introducing viscoelasticity, as seen from the plots, high velocity Lamb wave modes tend to S0 modes of the facesheet and shear modes to shear velocity in the facesheet. At a low frequency the limit coupling is not so pronounced but the tendency is that we have two characteristic velocities here: shear velocity of the core and flexural velocity of the facesheet (green dashed line in the Fig. 1). These two modes mainly determine the form of the dispersion curves at the low velocity limit.

It should be noted that attenuation increases very sharply in the frequency range where coupling takes place. This can be seen from simulations presented in Figure 3 when red dashed lines vanish due to the interaction between modes associated with viscoelasticity. The small interval in 1-10kHz is plotted to see how coupling between S0 and A1 arises with small viscoelasticity ($E'' = 0.01E'$). In this case standing modes transform into propagating modes with high attenuation in the frequency region of coupling. As can be seen from Fig. 3 attenuation increases practically in the order at the frequency region of 7.8 kHz where coupling takes place (dark dashed line).

A more simplified approach to investigation of wave propagation for SHM in CSP lies in using averaged over thickness parameters of the structures since we obtain 2D model in contrast to 3D theory considered above. In many cases, such approach is sufficiently good since it makes it possible to find a simpler analytical solution for propagating waves than the solution described by formulas (9),(10). The next section is devoted to the review of the Mindlin plate theory and the application of this approach to wave propagation modeling.

3. MINDLIN PLATE THEORY FOR SANDWICH STRUCTURES

In the Mindlin plate theory the displacements of the plate in the transverse, radial, and tangential direction components are expressed as follows (Mindlin & Deresiewicz, 1954)

$$w = w(r,\theta,t), u = z\psi_r(r,\theta,t), v = z\psi_\theta(r,\theta,t),$$

where *z* is the coordinate defining points across the thickness of the plate ($z = 0$ is the neutral plane**),** w is the out-of-plane displacement of the wave, ψ_r and ψ_θ are the rotations of vertical lines perpendicular to the mid-plane.

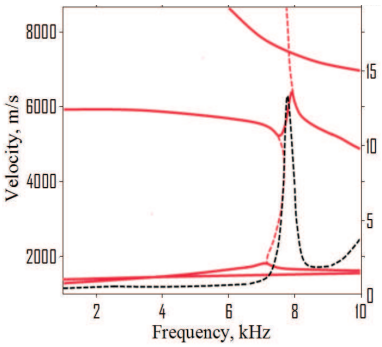

Figure 3: Dispersion curves of Lamb wave of phase velocities with respect to frequency for symmetric sandwich panel (red solid line corresponds to viscoelastic core $E' = 0.01E''$, dashed curve - elastic core $E'' = 0$, black dashed line is attenuation of the coupled mode, [Np/m]).

The governing equations for the symmetric honeycomb panels in terms of moments and shear forces can be presented based on shell approximation by the following approach (Rose & Wang, 2004)

$$\frac{1}{r}\frac{\partial Q_\theta}{\partial \theta} + \frac{\partial}{\partial r}Q_r + \frac{1}{r}Q_r - Q_\theta = \rho\frac{\partial^2}{\partial t^2}w\,, \qquad (14)$$

$$\frac{\partial M_{rr}}{\partial r} + \frac{1}{r}M_{rr} - \frac{1}{r}M_{\theta\theta} + \frac{1}{r}\frac{\partial}{\partial \theta}M_{r\theta} - Q_r = I\frac{\partial^2}{\partial t^2}\psi_r\,, \qquad (15)$$

$$\frac{1}{r}\frac{\partial M_{r\theta}}{\partial r} + \frac{2}{r}M_{r\theta} + \frac{1}{r}\frac{\partial}{\partial \theta}M_{\theta\theta} - Q_\theta = I\frac{\partial^2}{\partial t^2}\psi_\theta\,, \qquad (16)$$

where $\rho = \sum_{k=1}^{3}\int_{a_k}^{b_k}\rho_k dz$, is the mass density per unit area of the plate, index k corresponds to the material layer, ρ_k is the density, $I = \sum_{k=1}^{3}\int_{a_k}^{b_k}\rho_k z^2 dz$ is the mass moment of inertia. Each layer in the sandwich panel is bounded by the coordinates a_k and b_k in the thickness direction as shown in the Figure 4 (a). The stress resultants in terms of moments M_{rr}, $M_{\theta\theta}$, and $M_{r\theta}$, along with shear forces Q_r and Q_θ can be related to the transverse displacements and rotations as follows:

$$M_{rr} = \frac{D}{r}\left[r\frac{\partial \psi_r}{\partial r} + \nu(\psi_r + \frac{\partial \psi_\theta}{\partial \theta})\right], \qquad (17)$$

$$M_{r\theta} = \frac{D(1-\nu)}{2r}\left[\frac{\partial \psi_r}{\partial \theta} - \psi_\theta + r\frac{\partial \psi_\theta}{\partial r}\right], \qquad (18)$$

$$M_{\theta\theta} = \frac{D}{r}\left[\nu r\frac{\partial \psi_r}{\partial r} + \psi_r + \frac{\partial \psi_\theta}{\partial \theta}\right], \qquad (19)$$

$$Q_r = 2\kappa^2 G\left(\psi_r + \frac{\partial}{\partial r}w\right), \qquad (20)$$

$$Q_\theta = 2\kappa^2 G\left(\psi_\theta + \frac{1}{r}\frac{\partial}{\partial \theta}w\right), \qquad (21)$$

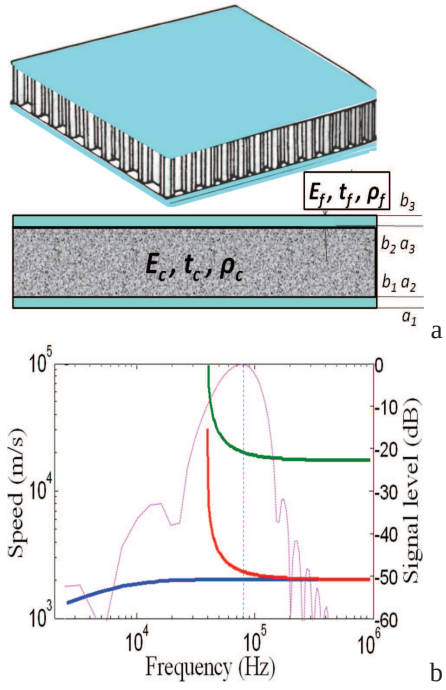

Figure 4: (a) - General view of the panel, (b) - Dispersion curves of the velocities with respect to frequency of symmetric sandwich panel in Mindlin approximation.

where $D = \frac{E_f t_f^3}{6} + \frac{E_c t_c^3}{12} + \frac{E_f t_f (t_f+t_c)^2}{4}$- is the flexural stiffness, ν is the Poisson ratio, which for the sake of simplicity is taken as equal for each layer, E_f, E_c are the Young's modulus of the facesheet and the core, correspondingly, t_f, t_c - thicknesses of the facesheet and the core layers, G is the shear stiffness of the plate, κ is the shear correction factor ˜1.

The general solution of the acoustic waves propagation with cycling frequency ω is $(w, \psi) = Re\left[(W, \Psi)\exp(-i\omega t)\right]$ (Rose & Wang, 2004), where and throughout this paper Re(.) denotes the real part of the quantity appearing in parentheses, ψ=(ψ_r,ψ_θ). The variables W, Ψ are presented by expressions

$$W = W_1 + W_2,$$
$$\Psi = \xi_1\nabla W_1 + \xi_2\nabla W_2 - e_z \times \nabla V,$$

where $\mathbf{e_z}$ is a unit vector in z direction (the displacement is $\mathbf{u_z}$=$w\mathbf{e_z}$, normal stress and strain in the thickness direction of the plate are not included in Mindlin plate theory), W_1, W_2, V satisfy three Helmholtz equations

$$\Delta W_1 + k_1^2 W_1 = 0, \qquad (22)$$
$$\Delta W_2 + k_2^2 W_2 = 0, \qquad (23)$$
$$\Delta V + k_3^2 V = 0 \qquad (24)$$

and Δ, ∇ - Laplace and Nabla operators, correspondingly. For isotropic sandwhich layers

$$k_{1,2}^2 = \frac{1}{2}(k_p^2 + k_s^2) \pm \sqrt{k_f^4 + \frac{1}{4}(k_p^2 - k_s^2)^2}, \quad (25)$$

$$k_3^2 = \frac{k_1^2 k_2^2}{k_p^2} \quad (26)$$

$$k_s = \omega/c_s, k_p = \omega/c_p, k_f = (\rho\omega^2/D)^{1/4},$$
$$c_s = (G/\rho)^{1/2}, c_p = (D/I)^{1/2}, \xi_j = (k_s/k_j)^2 - 1.$$

The dispersion curves for a typical sandwich panel corresponding to three branches are shown in the Figure 4 (b). The flexural wave corresponds to the real ω,k in whole ω domain. The second (and third) dilatation branch of (k,ω) dependence become real starting from the cutoff frequency.

For a similar 3D consideration we will consider a circular-patch actuator on the Mindlin plate generated by a surface traction plate waves in the form (Mindlin & Deresiewicz, 1954). In this case, the radially directed bending moments m_r, uniformly distributed along the ring of radius r_0 , can be described as follows:

$$m_r = \frac{1}{2} hp(t)\delta(r - r_0), \quad m_{r\theta} = 0,$$

where $p(t)$ is the amplitude of the force.

The source term for circular force leads to the solution for out-of-plane displacement

$$w(r, \omega) = s_1 H_0(k_1 r) + s_2 H_0(k_2 r), \quad (27)$$

where radius vector r is counted from the center of the actuator and coefficients s_1, s_2 are presented by

$$s_1 = \frac{i\pi hp(\omega)}{4D} \frac{k_1 r_0 J_1(k_1 r_0)}{k_1^2 - k_2^2},$$
$$s_2 = -\frac{i\pi hp(\omega)}{4D} \frac{k_2 r_0 J_2(k_2 r_0)}{k_1^2 - k_2^2},$$

where J_n and H_n are the Bessel and the Hankel functions of the first kind, respectively. We will consider that the frequency f of the source is sufficiently high ω=2πf>ωc, where ω_c is the cutoff frequency ω_c=(G/I)$^{1/2}$. As a result, the propagation spectrum is determined by two real wavenumbers k_1 and k_2. Expressions for rotations ψ=(ψ_r,ψ_θ) and, consequently, $u(r, \omega), v(r, \omega)$ can be found in the article (Mindlin & Deresiewicz, 1954).

4. DYNAMICS. TRANSIENT SOLUTION

To study the transient wave propagation we consider that the plate is excited by a pulse of the load stimulated by a PZT sensor (Raghavan & Cesnik, 2007). The expression for the wave pulses in the plane (x,y) may be derived from the steady-state solution in the frequency domain by applying the Fourier transform technique.

Let us consider that any pulse of the wave can be expanded into the Fourier transform which represents pulse as a series of plane waves. If the Fourier spectrum $G(\omega)$ of the signal $g(t)$ is

$$g(t) = \frac{1}{2\pi} \int_{-\infty}^{\infty} G(\omega) e^{-i\omega t} d\omega, \quad (28)$$

then the final solution for mechanical fields in the time domain will be

$$\begin{bmatrix} u^j(r,t,\theta) \\ v^j(r,t,\theta) \\ w^j(r,t,\theta) \end{bmatrix} = Re \frac{1}{2\pi} \int_{-\infty}^{\infty} G(\omega) \begin{bmatrix} u^j(\omega) \\ v^j(\omega) \\ w^j(\omega) \end{bmatrix} e^{-i\omega t} d\omega \quad (29)$$

For Mindlin plate theory we omit indices j. Let us present the results obtained by (29) and compare them with the results of the direct computer simulation of the real honeycomb plate. We consider the Hanning type actuation signals which are usually used for fault detection in SHM (Raghavan & Cesnik, 2007). The Hanning signal can be presented in the form

$$g(t) = [\Theta(t) - \Theta(t - 2\pi N/\omega_0)] [1 - \cos(\omega_0 t/N)] \sin(\omega_0 t) \quad (30)$$

where N is a parameter of impulse, f_0 =ω_0/2π is a carrier frequency, $\Theta(t)$ is the Heaviside step function. The selection of the driving frequency f was made in the frequency range from 20 to 100 kHz and this selection is critical for Lamb waves generation and fault detection.

We compare the analytical results with the corresponding results obtained by the Finite Element simulation. The FE modeling for 2D Mindlin plate is presented in Fig. 6. and it fits well with the theoretical approach. The main difference between these signals is that the theoretical results are valid for the infinite plate, and the FE 2D Mindlin plate model provides the result which takes into account reflections from the boundaries. The comparison of the 3D modeling of sandwich composite panels with the theoretical result is considered in the last section.

4.1 Propagation of the signal

As an example, for simulation we used Hunning pulses with 3.5 windowed input waveform with different carrying frequency f. The Fourier transform of such signal is presented in Fig. 5 a) for $f = 100kHz$ (dashed red line). Dispersion curves are presented in Fig. 5 (b) calculated according to the characteristic equation (11). It can be seen that the main domain of narrowband 3.5 windowed input waveform taking part in wave propagation is sufficiently broad (the domain between two red lines in dispersion curves Fig. 5 (b), which is taken, for example, on the level of 10 db Fig. 5 (a). The modes A_0 and S_0 of the facesheets are the leading ones in the formation of wave propagation through the structure. The

wave velocities $v = \omega/k$, were $\omega = 2\pi f$, k is a wavenumber, of the soft core are much lower than the facesheet velocities and that is why most dispersion curves have much lower slope than facesheet modes, except for the small vicinity of the facesheet modes A_0 and S_0. As a result, the generation of the Hanning windowed signal with leading frequency f ($f = 100kHz$ on the plot) leads to generation of antisymmetric and symmetric zeros modes of the facesheets coupled with a large number of local modes of the soft core.

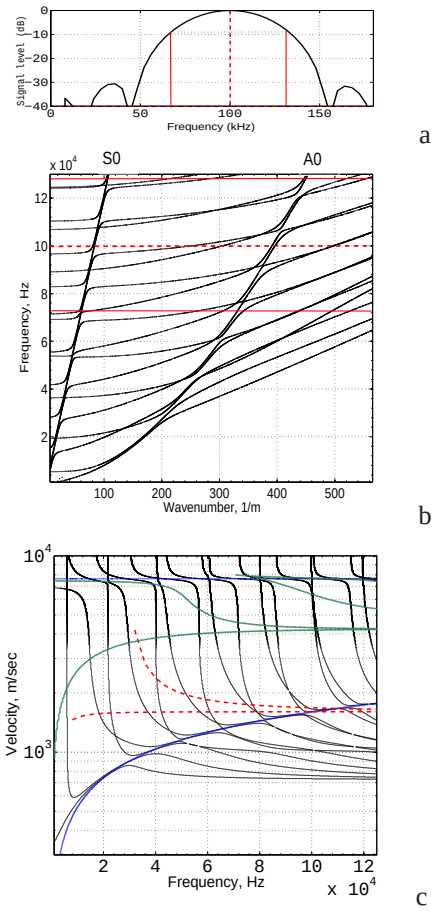

Figure 5: Dispersion relation for symmetric sandwich panel, (a) – Spectrum of the input signal for $f = 100kHz$, (b) – Honeycomb layered structure modes, (c) – Lamb velocities modes. (Blue lines - facesheet modes, red line - homogenized panel modes, dashed line - modes of Mindlin plate theory approach).

The phase velocities of the sandwich panel are presented in the Fig. 5 c (black lines) and correspond to the same dependencies $\omega = \omega(k)$ of the Fig. 5 (a). It can be easily seen that for the considered impute signal many modes propagate in the structures. If we consider the facesheet itself then only the S_0 mode and the A_0 mode can propagate in the considered frequency range below or at the order of $100kHz$ (blue lines in the Fig. 5 (c). In this region, the S_0 mode is almost non-dispersive, and the A0 mode is slightly dispersive. Considering the structure of the dispersion curves (Fig. 5 b) and velocity curves (Fig. 5 c) we can confirm that the majority of wavenumbers of the modes in dispersion curves are located in the small vicinity of A_0 and S_0 modes and in this case facesheet modes are much more sensitive to debond delamination defects than the core modes synchronizing vibration of the two facesheets.

For comparison, we will consider here the dispersion relations of Mindlin plate theory for symmetric sandwich structures (Dashed red line in Fig. 5 (c). The theory of the sandwich panels is considered in (Zenkert, 1995). We used analytical formulas from these sources just to identify coefficients in Mindlin plate theory used for investigation of wave propagation . The Mindlin plate theory approach shows that dispersion curves in the vicinity of f=100kHz are sufficiently close to the antisymmetric mode of the facesheet (Fig. 4).

Dispersion curves in coordinates (v, f) for homogenized plate are presented by green curves and they show quite different dispersion curves (Fig. 5c). In this case we can expect that a simplified approach can not completely describe wave propagation, and wave patterns in honeycomb structure are much more diverse. This is especially true for **a** high frequency excitation signal like 100kHz.

5. FINITE ELEMENT MODEL

The SCP has two main components, namely two stiff facesheets and a soft core between them. In addition to these subcomponents, we will consider an adhesive layer binding facesheets with the core. The thickness of the adhesive layer is generally sufficiently small but this component is important for simulation of the debond origination and growth. We also consider PZT actuator and sensors mounted on the panel. As a result of simulation, electrical signals of the sensors were compared with the signals obtained experimentally. Such approach best fits the typical sketch we have in SHM when the measured signals are used for interpretation of changes in monitored panels.

The FE model of the honeycomb sandwich structures with a piezoelectric actuator/sensor distribution is shown in Fig. 6. The model consists of the honeycomb core and two laminated facesheets with an actuator and sensors attached to the top sheet.

5.1 Facesheet

The facesheet in Abaqus can be modeled using shell, continuum shell, or solid element types (Fig. 7). We have found that continuum shell element type for the facesheet provides performance that is close to optimal. The facesheets were made by graphite/epoxy with lay-up sequence of [0/ 90]. In all cases, the composite layup is modeled explicitly as shown

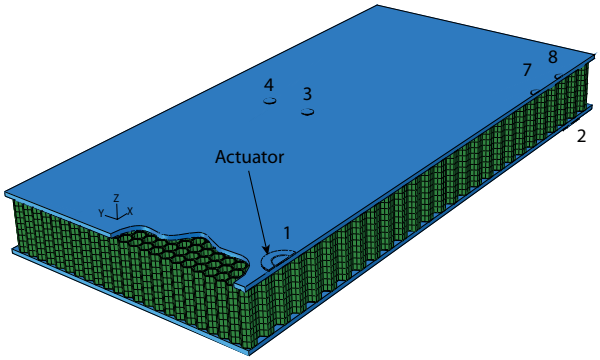

Figure 6: Finite element model of the sandwich honeycomb structure with a piezoelectric actuator (shown by an arrow) and a set of sensors (marked by the numbers).

Table 1: Parameters of the facesheet.

Ply elastic modulus E_{11}	16 Msi
Ply elastic modulus E_{22}	1.2 Msi
Ply Poisson's ratio ν_{12}	0.3
Ply shear modulus G_{12}	0.6 Msi
Ply thickness	6 mils
Laminate thickness	84 mils

in the figure 7. The parameters of the ply are shown in the table

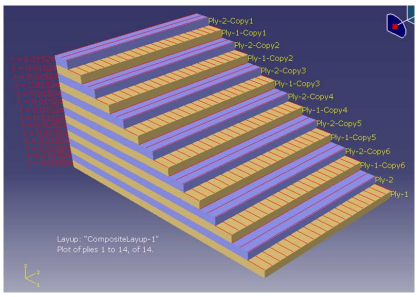

Figure 7: The composite layup of the facesheets consisting of 14 layers with orientation 0 and 90 degrees. The parameters of the lamina are shown in the Table1.

5.2 PZT sensors and actuators

Geometrical properties of PZT elements (Fig. 8) of the model are summarized in the Table2. The response of the PZT elements was determined by the piezoelectric stress matrix e and

Table 2: Parameters of the actuator and sensors.

Actuator diameter	0.709"
Actuator inner diameter	0.394"
Actuator thickness	20 mils
Sensor A diameter	0.354"
Sensor A thickness	20 mils
Sensor B diameter	0.250"
Sensor B thickness	10.5 mils

elasticity matrix c

$$[e] = \begin{bmatrix} 0 & 0 & -5.4 \\ 0 & 0 & -5.4 \\ 0 & 0 & 15.8 \\ 0 & 0 & 0.0 \\ 0 & 12.3 & 0.0 \\ 12.3 & 0 & 0.0 \end{bmatrix} [Cm^{-2}] \tag{31}$$

$$[c] = \begin{bmatrix} 12.1 & 7.54 & 7.52 & 0 & 0 & 0 \\ 7.54 & 12.1 & 7.52 & 0 & 0 & 0 \\ 7.52 & 7.52 & 11.1 & 0 & 0 & 0 \\ 0 & 0 & 0 & 2.26 & 0 & 0 \\ 0 & 0 & 0 & 0 & 2.11 & 0 \\ 0 & 0 & 0 & 0 & 0 & 2.11 \end{bmatrix} \times 10^{10}[Pa] \tag{32}$$

The dielectric matrix of the PZT material has the following diagonal elements $\varepsilon_{11} = \varepsilon_{22} = 8.11 \times 10^{-9}$ [C/V/m] and $\varepsilon_{33} = 7.35 \times 10^{-9}$ [C/V/m]. The density of the PZT material is $\rho_{PZT} = 7750$ [kg/m^3].

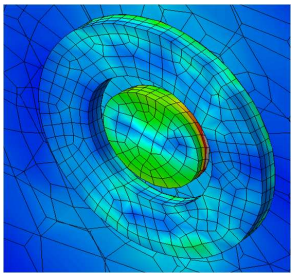

Figure 8: Snapshot of the actuator and sensor A during the simulations.

5.3 Honeycomb core

A special attention was paid to modeling of the detailed honeycomb structure (Fig. 9 a,b,c) including the difference in thickness for different walls of the structure and the presence of bending tips. The structure was built from a single strip shown in the Fig. 9(c). The bending tips were attached to the structure using the boolean operation on the mesh. The parameters characterizing mechanical properties of the honeycomb structure are listed in Tab. 3

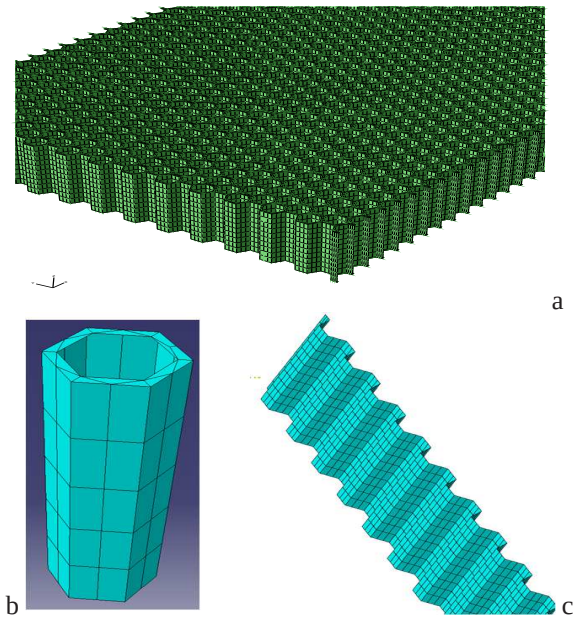

Figure 9: (a) Detailed view of the honeycomb structure. (b) A single cell of the structure with bending tips. (c) A single strip of the core used to build the structure.

Table 3: Parameters of the honeycomb core.

Cell size	0.25”
Shear modulus, ribbon direction (L)	70 ksi
Shear modulus, transverse direction (W)	40 ksi
Density	5.2 lbs/ft^3
Shear strength (L)	380 psi
Shear strength (W)	220 psi
Thickness	1”

The material properties of the Aluminum used to build the structure are the following: Young's modulus $E_{Alm} = 7.3084 \times 10^{10}$ [Pa], Poisson's ratio $\nu_{Alm} = 0.33$, Mass density $\rho_{Alm} = 2700$ [kg/m^3].

5.4 Adhesive layers

An important property of the honeycomb sandwich structure is the presence of adhesive layers both between the actuator/sensors and the facesheet and between the facesheet and the honeycomb core (Fig. 10). Accordingly, the layer with the following properties (Young's modulus $E_{Adh} = 4.82 \times 10^9$ [Pa], Poisson ratio $\nu_{Adh} = 0.40$, and mass density $\rho_{Adh} = 1255$ [kg/m^3]) was explicitly included into the finite element model.

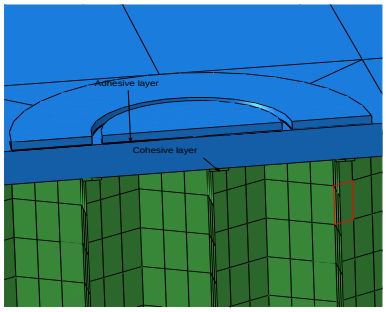

Figure 10: The location of the adhesive layer between PZT elements and facesheet and cohesive layer between facesheet and honeycomb.

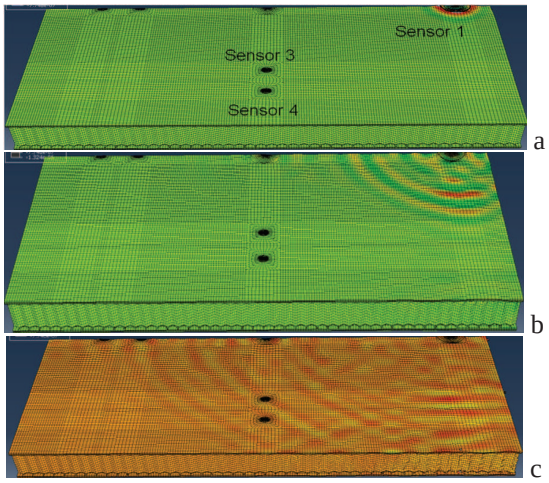

Figure 11: Finite element modeling of the sandwich honeycomb structure with a piezoelectric actuator. (a) – out-of-plane displacement for $t = 0.02ms$, (b) – $t = 0.06ms$, (c) – $t = 0.16ms$, (PZT sensors corresponding experimental layup are denoted black circles).

6. FE MODELING WAVE PROPAGATION

6.1 Numerical results

An experiment in Lamb wave propagation in a honeycomb sandwich panel was done by Metis Design Inc. in collaboration with ARC NASA. The sandwich panel fabricated for this test consisted of two 84-mil thick cross-ply carbon fiber composite laminates (bonded to a 1”- thick aluminum honeycomb core). The size of the panel was $1ft$x$1ft$. In the experiment, PZT sensors located on the facesheet of the honeycomb panel were used to determine the deformation at a different location (Fig. 6). The primary goal of this study is to model wave propagation field in $3D$ sandwich honeycomb panel to fit these results to SHM experimental data. Lamb wave tests were done over a frequency range from 20 to 100 kHz and 3.5-cycle Hanning windowed toneburst was used as

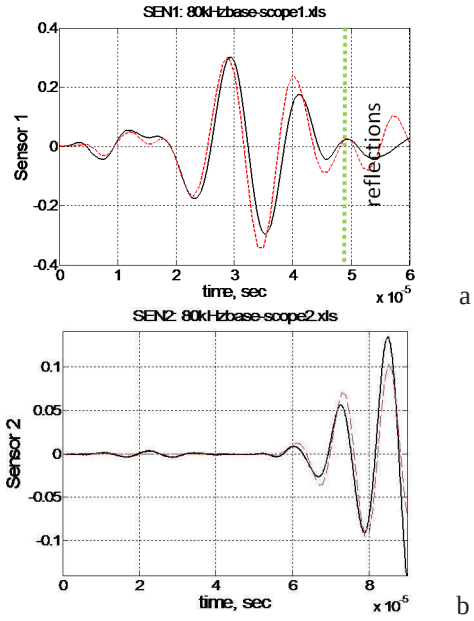

Figure 12: The results of the simulations of the wave propagation in honeycomb structure are shown in comparison with the experimental results measured for 80 kHz on (a) sensor # 1 embedded into actuator and (b) a similar sensor # 2 on the other side of the structure.

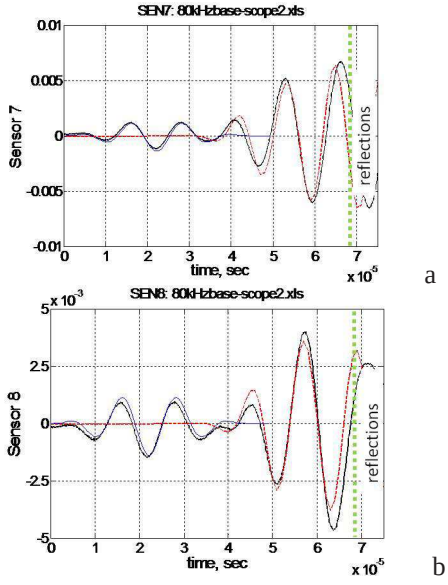

Figure 13: The results of the simulations of the wave propagation in honeycomb structure are shown in comparison with the experimental results measured for 80 kHz on (a) sensor # 7 and (b) sensor # 8.

an actuation signal for SHM.

First, we simulated a generation of acoustic modes by annular PZT patch and studied wave propagation. Second, different voltage generating signals were used to obtain transient fields which generate an electrical signal in a set of PZT sensors mounted on the facesheet plane in a particular experiment. Finally, we compared an electrical signal in pitch catch and pulse-echo technique and showed a very good agreement of both the theoretical and experimental data. Typical view of the FE simulations results is presented in Fig. 11. It can be easily seen from Fig. 11 that magnified displacement actuated by transducer located at the top of right-hand side corner propagates through the structure and generates electric signal in PZT sensors mounted to the top facesheet.

Results for voltage measurement for different sensors mounted on the plate are presented in Figures 12 and 13 for $f = 80kHz$, which shows the voltage on the corresponding sensors as a function of time at two locations, x = - 0.135m (y=6in) and x = 0.135m (y=6in), respectively, (the panel is centered at (0,0) and all sensors are positioned with respect to the center).

Theoretical and experimental results fit very well at the initial stage of wave propagation. The wave modes reflected from the boundaries of the plate lead to change in the phase of strain vibration and are not identical in the instance when we have reflections from the boundaries.

The results of simulations of the wave propagation in a honeycomb sandwich structure are shown in comparison with the experimental results for $f = 100kHz$ for a much longer time period, and they are presented in Fig. 14. You can see that when the time is longer we have stronger discrepancy between the theoretical and the experimental results even for the pristine panel without any damage. This is probably due to imperfections in the panel manufacturing and nonperfect boundary conditions in experiment in contrast to perfect geometry we use in numerical simulation.

7. CONCLUSION

We have investigated the wave propagation in sandwich honeycomb panels. A narrowband excitation waveform is employed to study wave propagation and damage detection in CSP. The new detailed model of SCP is developed. Computer simulation of the wave propagation is performed and results of the strains are compared with those obtained by experimental testing. For this the PZT sensors mounted on a composite facesheet plate are used. It has been demonstrated that initial stages of the propagating pulse practically always fit each other. For much longer time intervals many reflections from the boundaries change the phases of the strain oscillations, and it is not always possible to fit theoretical and experimental signals well. The conducted analysis has shown that in thick ($1in$ core) sandwich panels with Al honeycomb structure acoustic signal generated by the PZT actuator can be easily detected. Simulations have demonstrated practically the same response of the sensors we have in the experiment. The

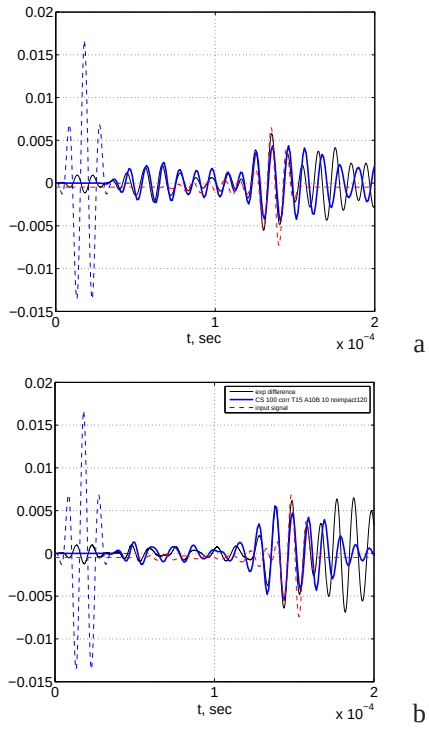

Figure 14: The results of the simulations of the wave propagation in honeycomb structure are shown in comparison with the experimental results measured for 100 kHz on (a) sensor # 3 and (b) sensor # 4. The blue line corresponds to FE modeling, Black one to experimental results and dashed red line to the modes calculated by Mindlin plate theory approach.

obtained results allow us to use FE methods for simulation of the acoustic waves propagating in the panel. The obtained results open up the prospect of the development of the SHM methods for advanced composite panels. This study makes it possible to deeper understand the physics based processes for the development of SHM methods. It should be pointed out that the FE model developed in this study has only been tested on one sample CSP and additional study will be necessary.

This paper addresses the different approaches to simulation of the guided wave propagation in sandwich structures with the emphasis given to the properties which can be used for SHM. The analytical investigation of dispersion curves, the plate wave using the Mindlin plate theory and the numerical simulations shows the main features we come across when developing real SHM methods. An analytical study is carried out to find the solution for transient wave propagation. The obtained analytical solutions are compared to the FE analysis as well as the experimental data.

REFERENCES

Bednarcyk, B., Arnold, S., Collier, C., & Yarrington, P. (2007). Preliminary Structural Sizing and Alternative Material Trade Study for CEV Crew Module.

Lowe, M. J. S. (1995). Matrix Techniques for Modeling Ultrasonic Waves in Multileyered Media. *IEEE Transactions on Ultrasonics, Ferroelectrics and Frequency Control*, *42*(1), 154-171.

Mindlin, R. D., & Deresiewicz, H. (1954). Thickness-shear and flexural vibrations of a circular disk. *Journal of applied physics*, *25*(6), 1328-1332.

Raghavan, A., & Cesnik, C. E. S. (2007). Review of guided-wave structural health monitoring. *The Shock and vibration digest*, *39*(1), 91-114.

Rose, R. F., & Wang, C. H. (2004). Mindlin plate theory for damage detection: Source solutions. *J. Acoust. Soc. Am.*, *116*(1), 154-171.

Zakharov, D. D. (2008). Orthogonality of 3D guided waves in viscoelastic laminates and far field evaluation to a local acoustic source. *International Journal of Solids and Structures*, *45*(1), 1788-1803.

Zenkert, D. (1995). *An Introduction to Sandwich Structures*.

Zenkert, D. (1997). *Ed. The Handbook of Sandwich Construction, EMAS Ltd, Warley, UK*.